Optimization strategies and artifacts of time-involved small-angle neutron scattering experiments[1]

Denis Mettus,[a]* Alfonso Chacon,[a] Andreas Bauer,[a,b] Sebastian Mühlbauer[c] and Christian Pfleiderer[a,b,d]

[a]Physik Department, Technische Universität München, Garching, Germany, [b]Centre for Quantum Engineering (ZQE), Technical University of Munich, D-85748 Garching, Germany, [c]Heinz Maier-Leibnitz Zentrum (MLZ), Technische Universität München, Garching, Germany, and [d]Munich Center for Quantum Science and Technology (MCQST), Technical University of Munich, D-85748 Garching, Germany. *Correspondence e-mail: denis.mettus@tum.de

Kinetic small-angle neutron scattering provides access to the microscopic properties of mesoscale systems under slow, periodic perturbations. By interlocking the phases of neutron pulse, sample modulation and detector signal, time-involved small-angle neutron scattering experiments (TISANE) allow one to exploit the neutron velocity spread and record data without major sacrifice in intensity at timescales down to microseconds. This article reviews the optimization strategies of TISANE that arise from specific aspects of the process of data acquisition and data analysis starting from the basic principles of operation. Typical artifacts of data recorded in TISANE due to the choice of time binning and neutron chopper pulse width are illustrated by virtue of the response of the skyrmion lattice in MnSi under periodic changes of the direction of the stabilizing magnetic field.

1. Introduction

Small-angle neutron scattering (SANS) is widely used as a probe of mesoscopic length scales up to several hundred nanometres in disciplines as diverse as material science, physics, chemistry and biology (Mühlbauer *et al.*, 2016, 2019; Dewhurst *et al.*, 2016; Wood *et al.*, 2018; Kohlbrecher & Wagner, 2000; Heenan *et al.*, 2006; Barker *et al.*, 2022; Glinka *et al.*, 1998). Providing reciprocal-space information, SANS is complementary to real-space and surface-sensitive imaging techniques, *e.g.* scanning tunneling, force, transmission electron and optical microscopy, or even electron holography. The growing need for information on the dynamic properties of mesoscale structures has motivated time-resolved SANS, resulting, more recently, in the development of time-involved small-angle neutron scattering experiments (TISANE) (Wiedenmann *et al.*, 2006; Kipping *et al.*, 2008). Targeting the dynamic response under a periodic drive, TISANE allows one to extend the time resolution of conventional SANS to well below sub-milliseconds at high scattering intensities.

In the light of the rapidly growing scientific and technological interest in mesoscale textures in quantum materials such as superconducting vortex matter, long-wavelength magnetic modulations, or skyrmion and meron lattices, a large number of scientific questions have recently emerged that may be addressed by means of time-resolved SANS studies. For instance, stroboscopic SANS has been used to study the vortex lattice dynamics in superconducting niobium (Mühlbauer *et al.*, 2011), showcasing the determination of the elasticity moduli, as well as vortex lattice relaxation and diffusion.
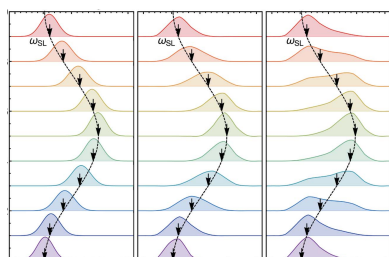
Similarly, TISANE has been used to track the unpinning of the skyrmion lattice in MnSi under periodic changes of field direction (Mühlbauer *et al.*, 2016). The excitation of Ni nanorod colloids under oscillating magnetic fields allowed the differences of response to be determined as a function of the amplitude and frequency of the driving field (Bender *et al.*, 2015). Recent studies (Glinka *et al.*, 2020) report utilization of TISANE for the study of hematite spindles in oscillating magnetic fields.

In this paper we review basic aspects of time-resolved SANS, focusing on optimization strategies of TISANE. Starting from the principles of operation, we discuss key elements of the data acquisition and analysis. Considering the example of skyrmion lattice kinetics in MnSi, we illustrate prominent artifacts associated with the choice of time binning and neutron pulse width.

2. Time-resolved SANS

2.1. Time-resolved SANS experiment with a continuous beam

Conventional SANS with a continuous beam permits slow changes of the scattering pattern to be resolved as a function of time. The associated time versus distance diagram is depicted in Fig. 1. A velocity selector (C) transmits a quasi-continuous beam of neutrons with a wavelength λ and a wavelength spread $\Delta\lambda/\lambda$. Typical neutron trajectories are represented by the solid and dashed lines, where the slope corresponds to the velocity of the neutrons, v_n, and the gray shaded areas reflect the distribution of velocities due to the wavelength spread $\Delta\lambda/\lambda$. The neutrons interact with a sample (S) which is subject to a periodic modulation with a period of modulation T_S, *e.g.* due to an AC magnetic field. Here, the
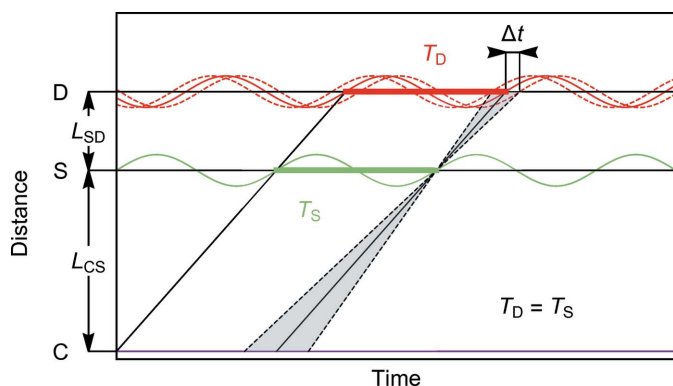

Figure 1
Time versus distance diagram of SANS with a continuous neutron beam. The velocity selector (C) generates a continuous beam with wavelength λ and wavelength spread $\Delta\lambda/\lambda$. Passing through the sample (S), the neutrons are recorded at the detector (D) as a function of time. The solid and dashed lines represent neutron trajectories, where the slope corresponds to the velocity of the neutrons. A periodic perturbation at the sample (green) depicts changes of the sample scattering intensity with period T_S. The oscillation at the detector (red) depicts changes of the recorded signal with a period $T_D = T_S$. The gray shaded area represents the distribution of neutron velocities associated with a wavelength spread $\Delta\lambda/\lambda$, which generates the time smearing of the detector signal characterized by Δt.

oscillation depicted in green at the sample position represents the periodic variation of the scattering by the sample as driven by the external modulation.

Following the scattering process, the neutrons are recorded at a detector (D) placed at a distance L_{SD} behind the sample. As a function of time, data recorded at the detector are binned with a period T_D. Neutrons that pass through the sample at a given phase of the sample modulation contribute to the detector signal at the same phase of the oscillation. In the idealized case, when all neutrons have the same velocity, v_n, the time dependence of the detector signal follows the time dependence of the sample modulation precisely, shifted by the time the neutrons need to travel the distance L_{SD}. Hence, in order to collect accurate data, the sample modulation and the detector data acquisition systems need to be synchronized such that $T_D = T_S$.

It is now instructive to consider typical velocity selectors used at SANS beamlines, which generate a triangular velocity distribution (Wagner *et al.*, 1992). This velocity distribution results in a spread of neutron trajectories as depicted by gray shading in Fig. 1, where the limiting velocities may be denoted v_{min} and v_{max}. For the purpose of the discussion, marked in gray shading and bounded by dashed lines are neutrons with velocities that pass through the sample at the same point of time as the modulation. These neutrons will arrive at the detector at different points of time. This causes an averaging of the detector signal as a function of time, where the time difference between the signal produced by neutrons with speed v_n and those with velocities v_{min} or v_{max} is given by

$$\Delta t = \frac{1}{2}\left(\frac{L_{SD}}{v_{min}} - \frac{L_{SD}}{v_{max}}\right) \simeq \frac{L_{SD}}{v_n}\left(\frac{\Delta\lambda}{\lambda}\right). \qquad (1)$$

Inserting values of typical SANS beamlines, $L_{SD} = 10$ m, $\lambda = 4.5$ Å and $\Delta\lambda/\lambda = 10\%$, one finds $\Delta t \simeq 1.14$ ms. Hence, in order to prevent significant averaging of the data recorded, the sample modulation should be chosen such that $T_S > 10\Delta t$, corresponding to frequencies of the sample modulation $f_S < 87.7$ Hz. By reducing the wavelength spread, Δt may be decreased, although at the expense of neutron flux.

2.2. Time-resolved SANS experiments with a pulsed beam

To improve the resolution in time-resolved SANS with minimal loss in intensity, a pulsed-beam technique proposed by R. Gähler (Kipping *et al.*, 2008), known as TISANE, may be used. The technique uses interlocking of the phases for neutron pulse, sample modulation and detector signal binning which allows a broad band of wavelengths to be used without degrading the time resolution.

Shown in Fig. 2 is the schematic layout of a TISANE instrument, *e.g.* as implemented at the SANS-1 beamline at FRM II. A velocity selector produces a continuous neutron beam with a wavelength λ and a wavelength spread $\Delta\lambda/\lambda$. Next, a chopper system generates neutron pulses with a repetition time T_C. The system used at SANS-1 consists of two discs placed at 50 mm distance from each other. Each chopper disc has boron-covered blades with 14 windows, each window

corresponding to an opening angle of 9.06°, and a set of magnetic bearings allowing chopper disc rotational speeds of up to 20 000 r min^{-1}. The system allows adjustment of disc rotation speed, direction and phase between the discs. Careful selection of these three parameters provides access to a wide range of T_C and allows tuning of the neutron pulse width while maintaining the desired pulse repetition time.

After the chopper, the neutrons pass through the sample which is placed at a distance L_{CS} behind the second chopper disc. The sample is subject to a periodic modulation with a period of oscillation T_S, e.g. generated by an AC magnetic field. Typical sample thicknesses are limited to below a few millimetres in order to avoid multiple scattering events. The neutrons are finally recorded with a period of time binning T_D at a detector placed at a distance L_{SD} behind the sample. The resulting data hence form a continuous time-resolved stream that is binned into a discrete number of time frames.

When the parameters L_{CS}, L_{SD}, T_C, T_S and T_D are chosen appropriately, all neutrons from different chopper pulses that arrive at the sample at the same point of time as the sample state oscillation, i.e. at the same phase, will reach the detector within the same phase (corresponding to the detector frequency) irrespective of their wavelengths. This is known as the TISANE condition. It requires that the chopper control electronics, the sample modulation system and the detector are synchronized at high accuracy, since a small deviation in the period of the oscillation will cause the phase shift to build up with increasing measurement time, averaging the scattering intensities as a result. To avoid any problems due to insufficient synchronization, a master trigger unit is used at SANS-1 (also known as the drive reference unit or DRU). Equipped with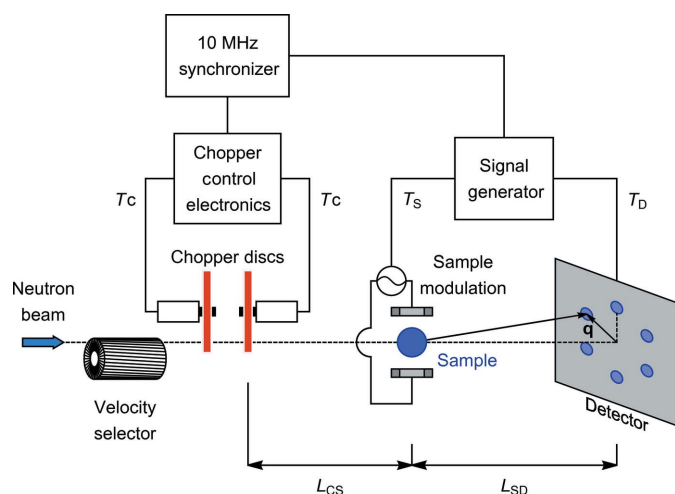 a high-precision quartz oscillator, the DRU transmits the reference signal with a base frequency of 10 MHz to the chopper system acting as a virtual master chopper of the AC magnetic field generator and the detector. As an alternative approach, bespoke electronics, referred to as the detector trigger generator (DTG), have been used (Glinka et al., 2020). It allows continuous monitoring of f_S and f_C, and recalculates f_D (where f stands for frequency of oscillation) required to satisfy the TISANE condition during the measurement. It is also worth mentioning work at the Spallation Neutron Source where the instrument was used in a time-of-flight mode (Adlmann et al., 2015). There, data were acquired in the event mode and synchronized on an absolute timescale with the sample modulation system. After the experiment, the data were processed using the correlation between the neutron events and the oscillatory cycle, and the detector signal rate was adjusted.

The TISANE condition may be illustrated in a time versus distance diagram as shown in Fig. 3(a). The continuous neutron beam is transformed into neutron pulses with repetition time T_C at the chopper (C). Neutrons passing through the sample (S), which is modulated at a period T_S, are recorded at the detector (D) with a period of time binning T_D.

Figure 2
Schematic depiction of the experimental setup used for TISANE as implemented at SANS-1 (FRM II). Following the velocity selector, a chopper generates neutron pulses with repetition time T_C. The neutrons pass through a sample subject to a periodic perturbation with a period of oscillation T_S. Neutrons are recorded at a detector with a period of time binning T_D. The scattered neutrons are characterized by the scattering vector **q**. The chopper control electronics, the sample modulation system and the detector are synchronized by the master trigger generator operating at 10 MHz.
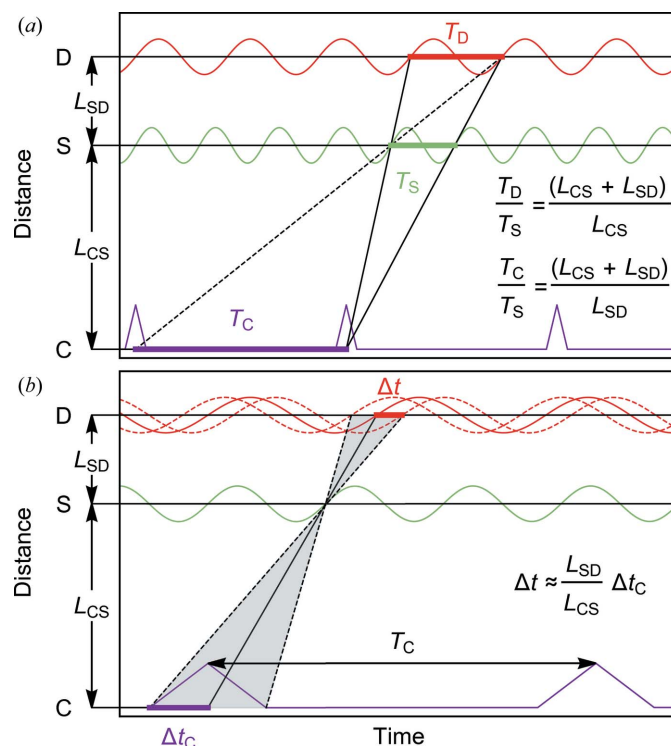
Figure 3
Time versus distance diagrams of TISANE. The chopper, sample and detector are denoted C, S and D, respectively. Lines represent neutron trajectories, where the slope corresponds to the velocity. A periodic perturbation of the sample (green) will cause a periodic oscillation of the neutron intensity at the detector (red). (a) Depiction of the TISANE condition. Neutrons with different velocities that start from the center of a chopper pulse reach the sample and the detector at the same phase of time dependence. (b) Signal smearing due to a finite chopper pulse width. The gray shaded area represents a distribution of neutrons with different velocities which arrive at the sample at the same phase of the modulation. Neutrons starting with the time difference Δt_C with respect to the center of the pulse reach the detector with delay Δt, causing a smearing.

Neutrons that start from the center of a chopper pulse and arrive at the sample at a given phase of the modulation will contribute to the same phase of the detector signal irrespective of the neutron velocity. Graphically, this is depicted in Fig. 3(a) for two neutrons starting from the same chopper pulse with different velocities (solid lines). In addition, neutrons from an earlier pulse (dashed line) must reach the sample and the detector also at the correct phase. Corresponding to this condition, the relations between T_D, T_C and T_S as determined by the distances between the chopper system, the sample and the detector are given by

$$\frac{T_D}{T_S} = \frac{L_{CS} + L_{SD}}{L_{CS}}, \qquad (2)$$

$$\frac{T_C}{T_S} = \frac{L_{CS} + L_{SD}}{L_{SD}}. \qquad (3)$$

As presented so far, the TISANE condition assumes infinitely narrow chopper pulses. However, the finite chopper pulse width Δt_C encountered in real experiments results in a distortion of the detector signal as illustrated in Fig. 3(b). Neutrons starting with a time difference from the pulse center will reach the detector shifted by this difference as weighted by L_{SD}/L_{CS}. Additional contributions Δt_S may arise from the averaging of the signal due to the finite flight time of the neutrons across the sample. In a similar manner, a contribution Δt_D may be expected from the finite thickness of the detector. The total time resolution at the detector is then given by (Wiedenmann et $al.$, 2006)

$$\Delta t^2 = \left(\Delta t_C \frac{L_{SD}}{L_{CS}}\right)^2 + \left(\Delta t_S \frac{L_{CS} + L_{SD}}{L_{CS}}\right)^2 + \Delta t_D^2. \qquad (4)$$

For typical chopper systems the values of Δt_C may vary between 50 and 500 µs. In comparison, typical sample thicknesses of a few millimetres correspond to $\Delta t_S \simeq 5$ µs. Typical diameters of the detector tubes of several millimetres correspond to $\Delta t_D \simeq 10$ µs. As a result, the time resolution of TISANE is essentially determined by the pulse width Δt_C.

2.3. Advantages and limitations of TISANE

A key advantage of the TISANE technique concerns the possibility of adjusting the time resolution and optimizing the beam intensity for increasing frequencies of the sample modulation. The details require careful consideration of the chopper duty cycle and frame overlap as discussed in this section. Assuming a chopper system that allows one to tune the pulse width independently from the pulse repetition time, it is convenient to define the ratio between the chopper pulse width and repetition time as the chopper duty cycle D_C:

$$D_C = \frac{\Delta t_C}{T_C}. \qquad (5)$$

Ignoring minor contributions by Δt_S and Δt_D, the time resolution of the instrument may hence be expressed as a function of the duty cycle:

$$\Delta t = D_C T_D = D_C \frac{L_{CS} + L_{SD}}{L_{CS}} T_S. \qquad (6)$$

Note that the changes of the scattering intensity observed at the detector are characterized by the period of the detector signal oscillation T_D rather than the period of the sample modulation T_S. Thus, for a given T_D, the signal quality may be inferred from D_C. This way, the frequency range accessible in the sample modulation is essentially limited by the maximum rotational speed of the chopper discs (until Δt_S and Δt_D become comparable to Δt_C). The approach is, however, limited by the neutron flux being proportional to the chopper duty cycle D_C. While increasing D_C past a certain value results in a decrease of the signal contrast due to insufficient time resolution, decreasing D_C would be at the expense of the intensity and would require longer measurement times to avoid hindering the signal contrast. For example, simulations for the case of a harmonically modulated sample scattering function yield an optimal chopper duty cycle value of 11% (Kipping et $al.$, 2008).

It is also possible to maximize the intensity by exploiting the spread of neutron velocities, since the time resolution remains unaffected as long as the TISANE condition is satisfied. Namely, when the spread of neutron velocity is sufficiently large, overlap between consecutive neutron pulses is reached such that neutrons that originate in different pulses pass through the sample at the same point of time. The number of chopper openings contributing to the sample intensity at a given instant in time is referred to as the overlap factor N_{OF}, given by

$$N_{OF} T_C = \frac{L_{CS}}{v_{min}} - \frac{L_{CS}}{v_{max}}. \qquad (7)$$

For $N_{OF} < 1$ the flux of neutrons at the sample is not constant. In this limit the detector signal may exhibit parasitic contributions due to, $e.g.$, residual Fourier terms of the chopper transmission function and the fundamental chopper and sample frequencies.

The scattering intensity recorded at the detector may be calculated as the product of the neutron velocity distribution function, F, the chopper transmission function, P_C, and the sample scattering function, S, integrated over all possible neutron velocities (Kipping et $al.$, 2008),

$$I_D(t, q) = I_0 \int_0^\infty F(v) P_C(t_C) S(t_S, q) \, dv, \qquad (8)$$

where the times at the chopper and the sample are corrected by the offsets $t_C = t - (L_{CS} + L_{SD})/v$ and $t_S = t - (L_{SD})/v$, respectively. The detector signal is here calculated neglecting variations of flight time due to the beam divergence and due to small-angle scattering.

An example of the intensities expected is depicted in Fig. 4(a). The distribution of neutron velocities was modeled by a triangular shape with $\lambda = 4.5$ Å and $\Delta\lambda/\lambda = 10\%$. The triangular chopper pulse function with $D_C = 0.15$ was approximated by a Fourier series. For modeling the oscillation of the scattering intensity of the sample a harmonic motion

was assumed with a frequency $f_S = 403.7$ Hz. The distances $L_{CS} = 23.9$ m and $L_{SD} = 10.0$ m were chosen in agreement with the configuration of the experiment discussed below and the frame overlap was $N_{OF} \simeq 0.65$.

Keeping the overlap factor N_{OF} well above unity should reduce the presence of undesired frequencies in the detector signal; in typical TISANE configurations it may be achieved at values exceeding $N_{OF} > 10$ (Kipping *et al.*, 2008). If sufficiently large values of N_{OF} are not accessible (*e.g.* for low sample modulation and hence chopper frequencies), parasitic signal components may be filtered out during the process of detector intensity averaging. The average intensity may be calculated in terms of a sum over several time constants T_D:

$$I_{avg}(t) = \frac{1}{n_{max}} \sum_{n=0}^{n_{max}} I_D(t + nT_D). \qquad (9)$$

The results of such an averaging are illustrated in Fig. 4(b). Typically in TISANE, data are always collected over a large number of detector periods for the sake of intensity, which would naturally filter out these 'parasitic' signal components. For the example considered here, the measurement times
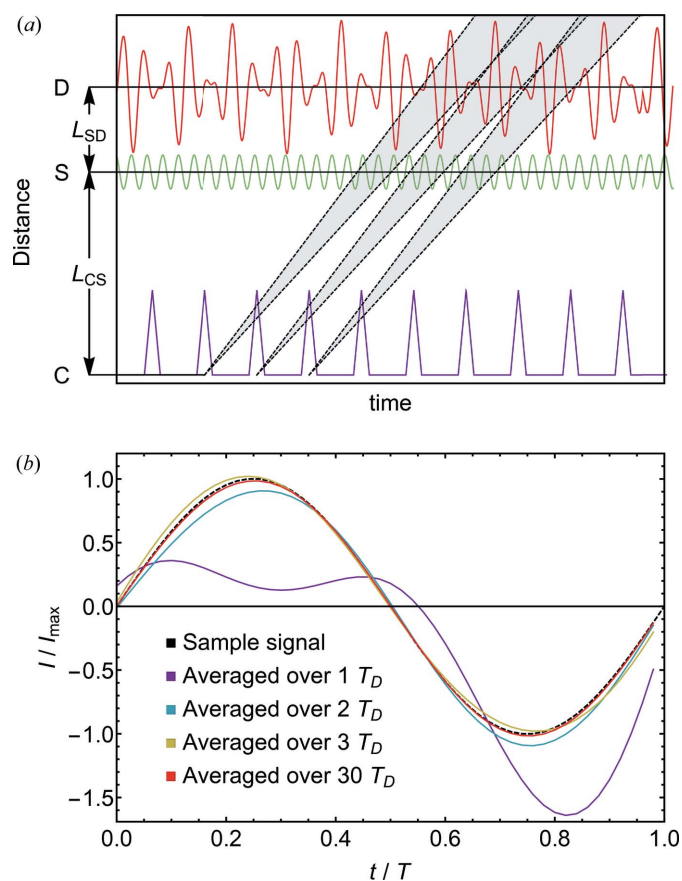
required for the experimental data shown in Fig. 6 were 120 s, with $f_D = 284.7075$ Hz, giving $n_{max} \simeq 3.4 \times 10^4$.

To summarize, the typical time resolution of TISANE is between 0.02 and 2.00 ms. For example, SANS-1 permits studies at sample oscillation frequencies up to $f_S \simeq 30$ kHz. The technique is designed to probe periodic changes in the neutron scattering pattern, but does not permit individual stochastic events to be resolved. While there are no strict limitations at lower frequencies, the TISANE advantage of time resolution being proportional to the period of detector signal oscillation becomes less prominent. Considering the intensity losses at the chopper system, one may argue that conventional time-resolved SANS with a continuous beam might be preferable for sample frequencies up to a few hundreds of Hz. A precise comparison of the techniques may be possible when comparing equation (1) with equation (6). It would depend on various details of implementation, notably beam intensity, desired momentum resolution, range of available neutron wavelengths *etc.*

3. Parasitic signal contributions

3.1. TISANE of the skyrmion lattice motion in chiral magnets

In the following we present TISANE data recorded in a kinetic neutron scattering study of the skyrmion lattice (SL) motion in chiral magnets. Skyrmions are topologically non-trivial spin textures that exhibit an exceptionally efficient coupling to spin currents, notably spin-polarized charge currents and magnon currents (Schulz *et al.*, 2012; Everschor *et al.*, 2012; Mochizuki *et al.*, 2014; Zhang *et al.*, 2018). The data we report here follow up on an investigation carried out at the SANS beamline V4 at Helmholtz-Zentrum Berlin (Mühlbauer *et al.*, 2016). The work reported here concerned the information content and putative presence of parasitic signal contributions at large excitation amplitudes, when the skyrmion lattice follows the oscillatory motion of the field direction.

The experiment was carried out at the beamline SANS-1 at FRM-II, Garching, Germany (Mühlbauer *et al.*, 2016). Unpolarized neutrons were used with a wavelength of $\lambda = 4.5$ Å and a wavelength spread $\Delta\lambda/\lambda \sim 10\%$ (FWHM). The collimation distance was set to 12 m, the sample–detector distance was $L_{SD} = 10.025$ m and the chopper–sample distance was $L_{CS} = 23.925$ m. The chopper system was operated in a mode where one chopper disc was spinning while the second chopper disc was kept in a fixed position. With each chopper disc having 14 openings and each opening having an angular width of $9.06°$, this resulted in a chopper duty cycle of $D_C = 0.352$.

A spherical single crystal of MnSi with a diameter of 5.8 mm was studied. The spherical sample shape served to ensure uniformity of demagnetizing and hence internal fields (Adams *et al.*, 2011). The oscillatory motion of the direction of the applied magnetic field was generated by means of the superposition of crossed DC and AC fields, each produced by a set of Helmholtz coils. The static magnetic field was $B_{dc} = 170$ mT. The amplitude of the oscillating magnetic field was $B_{ac} = $

Figure 4
Effect of the low frame overlap on the detector signal. (*a*) Time versus distance diagram for $N_{OF} \simeq 0.65$. Insufficient frame overlap results in a strongly varying beam intensity at the sample, causing additional components in the detector signal. (*b*) Averaged detector signal for different measurement durations. The dashed black line represents the original sample signal. The colored lines show detector signals averaged over multiple periods T_D as stated in the legend.

6.11 mT at a frequency f_S = 403.7075 Hz. In order to account for shielding of the AC magnetic field by the cryostat and instrument components, the magnetic field was calibrated with a Hall probe at room temperature. The sample was cooled to the skyrmion lattice phase at T = 28.0 K by means of a closed-cycle cryostat equipped with a quartz vacuum shield. Additional heating effects due to the AC field were carefully compensated.
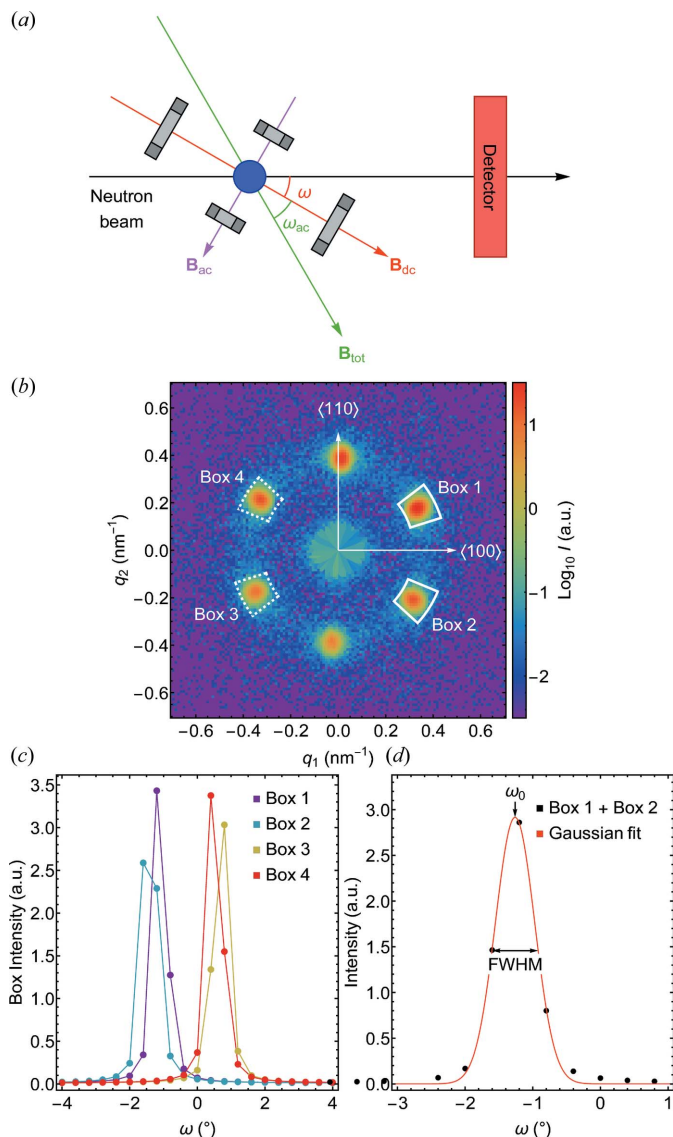

Figure 5
Basic aspects of TISANE in the skyrmion lattice of MnSi. (a) The static magnetic field $\mathbf{B}_{dc}$ and the oscillating magnetic field $\mathbf{B}_{ac}$ were generated by Helmholtz coils depicted in gray shading. The orientation of the resulting magnetic field $\mathbf{B}_{tot}$ with respect to $\mathbf{B}_{dc}$ is denoted by the angle ω_{ac}. The orientation of the static field with respect to the incident neutron beam is denoted by the rocking angle ω. (b) Typical SANS intensity pattern of the skyrmion lattice in MnSi as stabilized by a static magnetic field $\mathbf{B}_{dc}$ (no $\mathbf{B}_{ac}$ present). Crystallographic ⟨110⟩ and ⟨100⟩ axes were vertical and horizontal, respectively. Boxes 1, 2, 3, 4 denote detector segments in which scattering intensity was observed. (c) Typical integrated scattering intensity recorded in the boxes marked in panel (b) as a function of ω. (d) Average intensity recorded in boxes 1 and 2. The red line represents a Gaussian fit of the data, with ω_0 denoting the rest position of the skyrmion lattice in the absence of an AC field.

A schematic depiction of the experimental setup is shown in Fig. 5(a), featuring the direction of the incident neutron beam, the sample, the magnetic static and oscillating magnetic fields $\mathbf{B}_{dc}$ and $\mathbf{B}_{ac}$, and the detector. A static field, $\mathbf{B}_{dc}$, needed to stabilize the skyrmion lattice phase was generated by a set of Helmholtz coils depicted in gray shading. The direction $\mathbf{B}_{dc}$ was tilted with respect to the incident neutron beam by the rocking angle ω. The oscillation of the direction of the magnetic field was generated with a small AC field, $\mathbf{B}_{ac}$, aligned perpendicular to the DC field. The direction of the resulting total magnetic field $\mathbf{B}_{tot}$ with respect to $\mathbf{B}_{dc}$ is characterized by the angle ω_{ac}. The sample was aligned in such a way that the vertical axis of the system was parallel to a crystallographic ⟨110⟩ direction, and the direction of the DC field $\mathbf{B}_{dc}$ coincided with another ⟨110⟩ crystallographic direction.

Shown in Fig. 5(b) is a typical sixfold intensity pattern of the skyrmion lattice in the absence of the AC field (Mühlbauer *et al.*, 2009). The pattern was recorded at $\omega = -0.4°$, corresponding to the zero position. The diffuse intensity contributions in the background were visible on a logarithmic scale only; they are very weak and may be ignored in what follows. For TISANE, four peaks were selected, as marked by the boxes denoted 1–4. Typical integrated intensities recorded in these boxes as a function of rocking angle are shown in Fig. 5(c). The two remaining peaks at the top and the bottom were not tracked as they do not depend on ω.

Comparison of the intensities in the four boxes underscores the sensitivity of the scattering intensity to the precise orientation between the sample, neutron beam and the magnetic field. In the case of a perfectly aligned system, Fig. 5(c) should exhibit symmetry around $\omega = 0$: curves for boxes 1 and 4 and boxes 2 and 3 should cross at $\omega = 0$, and respective curves for boxes 1 and 2 and boxes 3 and 4 should overlap. To compensate for the small misalignment, we considered the sum of the intensities of box 1 and box 2 as a function of ω, as shown in Fig. 5(d). The resulting curve may be described well with a Gaussian featuring an FWHM = 0.68°. The shape and the width of the curve reflect the mosaicity of the SL structure. The area under the curve is proportional to the volume fraction of SL phase. The position of the peak center at $\omega_0 = -1.27°$ represents the orientation of the SL in the absence of the AC magnetic field. Tracking deviations of the peak position permitted us to track changes of the SL direction.

To determine time-dependent rocking scans we recorded at first the scattering intensity for selected fixed rocking angles $\omega - \omega_0$ as a function of time. Data were then sorted into a number of intervals according to different points of time during a full period of the oscillation. Note that the data were recorded at the detector with the period of oscillation T_D. By plotting the intensity as a function of t/T_D it was possible to relate the intensity variations to the modulation of the sample state characterized by t_S/T_S; therefore we omit the notations and present the data for different t/T. The sum of the intensities of boxes 1 and 2 [see Fig. 5(b)] as a function of time is shown in Fig. 6(a). The color shading denotes different rocking angles $\omega - \omega_0$. The two-dimensional time-resolved rocking

map generated on the basis of these data is shown in Fig. 6(b). Here horizontal lines correspond to specific rocking angles and the colors correspond to those used in Fig. 6(a).

In order to extract the rocking curves for a sequence of different time frames, the two-dimensional rocking map was transposed as shown in Fig. 6(c). This way data are presented as a function of t/T. The horizontal lines mark time frames rather than rocking angles. The resulting rocking curves are depicted in Fig. 6(d) where the colored lines denote the time frames marked in Fig. 6(c). Taken together, these time-resolved TISANE rocking curves are the result of a comprehensive data set, noting that a correct arrangement of time and rocking angles is essential.

At first sight, Fig. 6(d) appears to show that the SL follows the direction of B_{tot}, where the instantaneous field direction is marked by an arrow. In comparison with the Gaussian rocking curve observed without oscillation of the field direction shown in Fig. 5(d), the intensities are, however, heavily broadened, seemingly shifting between two prominent maxima. As
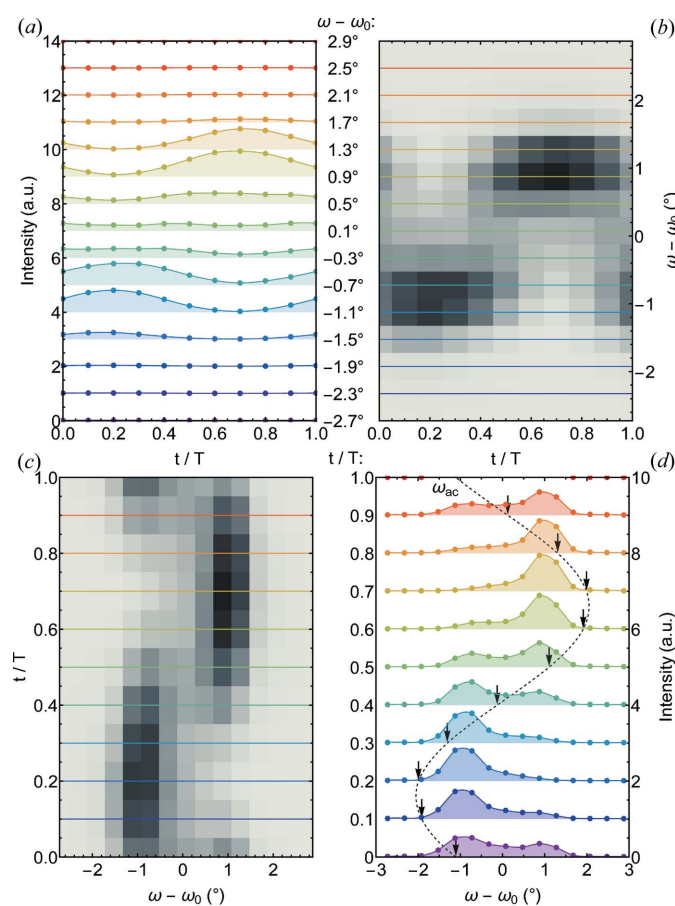
discussed in the next section, both the qualitative and quantitative forms of the TISANE rocking curves are purely parasitic effects that originate in the specific choice of parameters of data binning and pulse length used here.

3.2. Consequences of data binning and pulse length

To gain insight into the origin of the TISANE rocking curves shown in Fig. 6(d), different basic responses of the SL motion were calculated assuming that the whole SL volume simultaneously and instantly followed changes of the magnetic field direction as described by ω_{ac} (Fig. 7). In addition it was assumed that the SL order was characterized by a Gaussian distribution that was not affected by the motion. Quantitative values of the Gaussian rocking intensity as well as the size of $\mathbf{B}_{ac}$ corresponded to those observed in the study of MnSi shown in Figs. 5 and 6.

It proves to be instructive to consider at first three fundamental oscillatory time dependences, namely a sinusoidal, a triangular and a square motion, depicted in the top, middle and bottom rows of Fig. 7, respectively. As shown in the panels on the left-hand side of Fig. 7, without binning the data as a function of time, the Gaussian distributions follow any changes of field direction instantly without change of width or intensity. In comparison, panels on the right-hand side of Fig. 7 depict TISANE rocking scans when binning the time dependence into ten time frames. Within each time frame, t_i, all scattering data were thereby integrated from t_i to t_{i+1}:

$$I(\omega - \omega_0)|_{t=t_i} = \frac{1}{t_{i+1} - t_i} \int_{t_i}^{t_{i+1}} I(\omega - \omega_0, \tau)\, d\tau. \qquad (10)$$

As evident in the panels on the right-hand side of Fig. 7, the binning generated an averaging and concomitant smearing. For the sinusoidal motion, shown in Fig. 7(b), both the peak height and peak width vary periodically as a function of time, where the height and width scale with the rate of change of the field orientation. Accordingly, for the triangular time dependence shown in Fig. 7(d) the smearing was essentially the same for all time frames, as the absolute value of the rate of change of the field direction was essentially constant. Contributions by points of time where changes of the direction of motion occurred were averaged out. The rectangular motion, finally, exhibits a broadening and a double-peak structure in the vicinity of those points of time at which instant changes of field orientation occurred, as shown in Fig. 7(f). While the binning into time frames did not affect the appearance of the TISANE rocking scans radically, the effect was inevitable and important to keep in mind. Indeed, the impact of the binning may be reduced by increasing the number of time frames, although this is at a significant cost of intensity for each time frame. It seems logical to select the number of time bins N_{bin} at least high enough so that the duration of a single time bin T_D/N_{bin} is less than the instrumental resolution defined in equation (6).

Comparing the calculated rocking scans shown in Fig. 7(b) with the experimental data shown in Fig. 6(d), the general trend of a broadening that scales with the rate of change of the

Figure 6
Acquisition process of time-resolved rocking scans. (a) Sum of the positions of rocking angle $\omega - \omega_0$ as denoted on the right-hand side. Data have been shifted vertically for clarity. (b) Two-dimensional time-resolved rocking map inferred from panel (a). Horizontal lines correspond to specific rocking angles where the color coding is that of panel (a). (c) Transposed two-dimensional intensity map of the map shown in panel (b). Horizontal lines denote time frames. (d) Rocking peaks for different time frames. The dashed line represents the variation of the field direction ω_{ac}. The arrows mark the value of ω_{ac} for each respective time bin. Data are shifted vertically for clarity.

field direction under sinusoidal motion cannot be ruled out. Yet, the experimental data exhibit a pronounced double-peak structure with maxima that are essentially located at two fixed rocking angles $\omega - \omega_0 \simeq \pm 1°$ and scattering intensity that
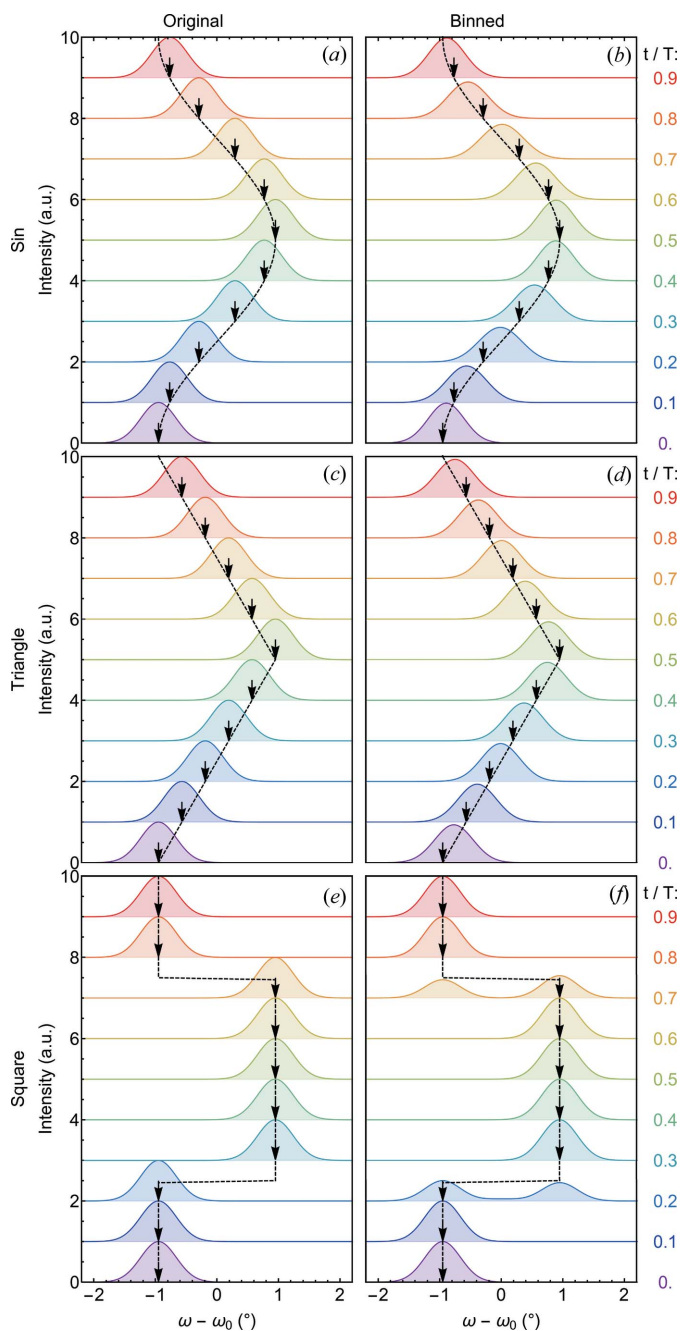
appears to be shifted between these two maxima as a function of time.

For the experimental parmeters chosen here, it transpires that the double-peak structure may be fully attributed to the choice of neutron pulse length affecting the time resolution defined in equation (6). Considering a chopper made of two discs with rectangular windows, a triangular pulse shape with duty cycles typically ranging between 0.10 and 0.35 is obtained. In the case of a chopper pulse that is too wide, details of the signal will get heavily averaged out and the shape of the TISANE rocking scans will become symmetric. For a detailed assessment of the influence of the pulse shape and duty cycle on the appearance of the TISANE rocking scans, the intensities may be estimated with equation (8). For our calculations, we assumed that the TISANE condition is strictly obeyed; hence the wavelength spread did not affect the time smearing of the detector signal. Additionally we considered measurement times long enough that $n_{max} \rightarrow \infty$ when the averaged detector signal was calculated according to equation (9). With that, in our calculations the wavelength spread could be approximated as a delta function, and the TISANE rocking intensity could be estimated as the convolution of the chopper pulse function, P_C, with the sample scattering function, S, namely

$$I_{avg}(\phi) = I_0 \int_0^{2\pi} P_C(\Delta\phi)\, S(\phi + \Delta\phi)\, d\Delta\phi. \qquad (11)$$

Shown in Fig. 8 is an evaluation of the influence of the pulse length for chopper duty cycles $D_C = 0$, 0.15 and 0.35. For ease of comparison, shown in Fig. 8(a) is the behavior without
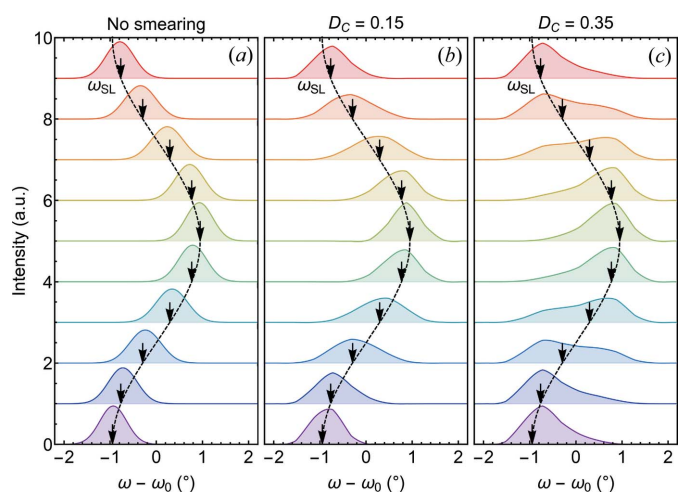
Figure 7
Changes of simulated TISANE rocking intensities due to binning in time frames. Data have been shifted vertically for clarity. Panels on the left-hand side assume a Gaussian intensity distribution that follows accurately a given periodic time dependence without binning. Panels on the right-hand side display the effects of time smearing when binning data in ten time frames. Color shading depicts specific time frames. (a), (b) Behavior for a sinusoidal oscillation. The binning results in a broadening and concomitant reduction of peak height. (c), (d) Behavior for a triangular motion. The binning essentially results in the same broadening and peak reduction for all time frames. (e), (f) Behavior for a rectangular oscillation. A double peak emerges for time frames of fast changes.

Figure 8
Changes of simulated TISANE rocking intensities due to binning for different duty cycles. Data have been shifted vertically for clarity. (a) Gaussian rocking curves that follow a sinusoidal driving field without binning and time smearing. (b) Gaussian rocking curves that follow a sinusoidal oscillation taking into account a TISANE duty cycle $D_C = 0.15$ and binning into ten time frames. A broadening and a reduction of the Gaussian distribution appear to be present. (c) Gaussian rocking curves that follow a sinusoidal oscillation taking into account a TISANE duty cycle $D_C = 0.35$ and binning into ten time frames. Besides an apparent broadening and reduction of the Gaussian distribution, a double-peak structure emerges due to the binning.
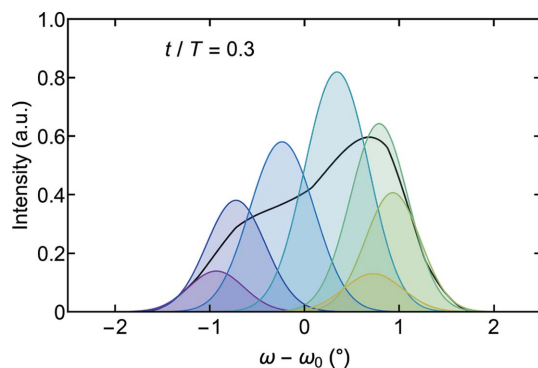
Figure 9
Origin of the double-peak structure in TISANE rocking scans for a long neutron pulse corresponding to a duty cycle of $D_C = 0.35$. The black line represents the TISANE rocking scan shown in Fig. 8(c) for a time frame $t/T = 0.3$. Color-shaded Gaussians represent scattering contributions scaled by the chopper pulse function as associated with different time frames due to the long chopper pulse.

binning and with a vanishingly small value of D_C. In this limit the TISANE rocking intensity follows any changes in ω_{ac} while maintaining the peak shape and height as already shown in Fig. 7(a). Considering now $D_C = 0.15$ [Fig. 8(b)] the combined effect of binning and finite pulse length causes an averaging akin to that shown in Fig. 7(b). Finally, for $D_C = 0.35$, the calculated TISANE rocking curves shown in Fig. 8(c) exhibit the double-peak behavior observed experimentally. As the experimental data shown in Fig. 6(d) were measured for a chopper duty cycle $D_C = 0.352$ this provides a full account of the double-peak structure.

On an intuitive level the double-peak distribution may be understood as a parasitic superposition of rocking curves due to the wide chopper pulse width. Shown by the black line in Fig. 9 is the TISANE rocking curve displayed in Fig. 8(c) for $t/T = 0.3$. This curve may be understood as a normalized sum of Gaussian intensity profiles that originate at different times within the pulse. The color shading here corresponds to the time frames shown in Fig. 8(c). In other words, the pulse width effectively includes contributions associated with several time frames weighted by the triangular pulse shape at the respective moments of time.

4. Summary

In summary, we reviewed optimization strategies of TISANE in kinetic SANS studies of mesoscale textures. To illustrate parasitic effects we considered the motion of the SL in MnSi under oscillations of the field direction, focusing on the emergence of pronounced qualitative and quantitative changes of the intensity distribution, notably strong velocity-dependent broadening and a double-peak structure suggestive of periodic shifts of scattering intensity. Simulating the effects of binning into time frames for different duty cycles for a Gaussian rocking distribution that is driven by a sinusoidal, triangular and square wave excitation, we reproduce the behavior observed experimentally. This illustrates the potential of TISANE to obtain time-resolved information at high

scattering intensities, while emphasizing the need for carefully simulating and choosing key parameters of data detection and analysis.

References

Adams, T., Mühlbauer, S., Pfleiderer, C., Jonietz, F., Bauer, A., Neubauer, A., Georgii, R., Böni, P., Keiderling, U., Everschor, K., Garst, M. & Rosch, A. (2011). *Phys. Rev. Lett.* **107**, 217206.

Adlmann, F. A., Gutfreund, P., Ankner, J. F., Browning, J. F., Parizzi, A., Vacaliuc, B., Halbert, C. E., Rich, J. P., Dennison, A. J. C. & Wolff, M. (2015). *J. Appl. Cryst.* **48**, 220–226.

Barker, J., Moyer, J., Kline, S., Jensen, G., Cook, J., Gagnon, C., Kelley, E., Chabot, J. P., Maliszewskyj, N., Parikh, C., Chen, W., Murphy, R. P. & Glinka, C. (2022). *J. Appl. Cryst.* **55**, 271–283.

Bender, P., Günther, A., Honecker, D., Wiedenmann, A., Disch, S., Tschöpe, A., Michels, A. & Birringer, R. (2015). *Nanoscale*, **7**, 17122.

Dewhurst, C. D., Grillo, I., Honecker, D., Bonnaud, M., Jacques, M., Amrouni, C., Perillo-Marcone, A., Manzin, G. & Cubitt, R. (2016). *J. Appl. Cryst.* **49**, 1–14.

Everschor, K., Garst, M., Binz, B., Jonietz, F., Mühlbauer, S., Pfleiderer, C. & Rosch, A. (2012). *Phys. Rev. B*, **86**, 054432.

Glinka, C. J., Barker, J. G., Hammouda, B., Krueger, S., Moyer, J. J. & Orts, W. J. (1998). *J. Appl. Cryst.* **31**, 430–445.

Glinka, C., Bleuel, M., Tsai, P., Zákutná, D., Honecker, D., Dresen, D., Mees, F. & Disch, S. (2020). *J. Appl. Cryst.* **53**, 598–604.

Heenan, R. K., King, S. M., Turner, D. S. & Treadgold, J. R. (2006). Proceedings of the 17th Meeting of the International Collaboration on Advanced Neutron Sources, 25–29 April 2005, Santa Fe, New Mexico, USA, pp. 780–785.

Kipping, D., Gähler, R. & Habicht, K. (2008). *Phys. Lett. A*, **372**, 1541–1546.

Kohlbrecher, J. & Wagner, W. (2000). *J. Appl. Cryst.* **33**, 804–806.

Mochizuki, M., Yu, X. Z., Seki, S., Kanazawa, N., Koshibae, W., Zang, J., Mostovoy, M., Tokura, Y. & Nagaosa, N. (2014). *Nat. Mater.* **13**, 241–246.

Mühlbauer, S., Binz, B., Jonietz, F., Pfleiderer, C., Rosch, A., Neubauer, A., Georgii, R. & Böni, P. (2009). *Science*, **323**, 915–919.

Mühlbauer, S., Heinemann, A., Wilhelm, A., Karge, L., Ostermann, A., Defendi, I., Schreyer, A., Petry, W. & Gilles, R. (2016). *Nucl. Instrum. Methods Phys. Res. A*, **832**, 297–305.

research papers

Mühlbauer, S., Honecker, D., Périgo, A., Bergner, F., Disch, S., Heinemann, A., Erokhin, S., Berkov, D., Leighton, C., Eskildsen, M. R. & Michels, A. (2019). *Rev. Mod. Phys.* **91**, 015004.

Mühlbauer, S., Kindervater, J., Adams, T., Bauer, A., Keiderling, U. & Pfleiderer, C. (2016). *New J. Phys.* **18**, 075017.

Mühlbauer, S., Pfleiderer, C., Böni, P., Forgan, E. M., Brandt, E. H., Wiedenmann, A., Keiderling, U. & Behr, G. (2011). *Phys. Rev. B*, **83**, 184502.

Schulz, T., Ritz, R., Bauer, A., Halder, M., Wagner, M., Franz, C., Pfleiderer, C., Everschor, K., Garst, M. & Rosch, A. (2012). *Nat. Phys.* **8**, 301–304.

Wagner, V., Friedrich, H. & Wille, P. (1992). *Physica B*, **180–181**, 938–940.

Wiedenmann, A., Keiderling, U., Habicht, K., Russina, M. & Gähler, R. (2006). *Phys. Rev. Lett.* **97**, 057202.

Wood, K., Mata, J. P., Garvey, C. J., Wu, C.-M., Hamilton, W. A., Abbeywick, P., Bartlett, D., Bartsch, F., Baxter, P., Booth, N., Brown, W., Christoforidis, J., Clowes, D., d'Adam, T., Darmann, F., Deura, M., Harrison, S., Hauser, N., Horton, G., Federici, D., Franceschini, F., Hanson, P., Imamovic, E., Imperia, P., Jones, M., Kennedy, S., Kim, S., Lam, T., Lee, W. T., Lesha, M., Mannicke, D., Noakes, T., Olsen, S. R., Osborn, J. C., Penny, D., Perry, M., Pullen, S. A., Robinson, R. A., Schulz, J. C., Xiong, N. & Gilbert, E. P. (2018). *J. Appl. Cryst.* **51**, 294–314.

Zhang, S. L., Wang, W. W., Burn, D. M., Peng, H., Berger, H., Bauer, A., Pfleiderer, C., van der Laan, G. & Hesjedal, T. (2018). *Nat. Commun.* **9**, 2115.